CrossMark

Parametric Optimization of Thermoelectric Generators for Waste Heat Recovery

SHOUYUAN HUANG[1] and XIANFAN XU[1,2]

1.—School of Mechanical Engineering and Birck Nanotechnology Center, Purdue University, West Lafayette, IN, USA. 2.—e-mail: xxu@ecn.purdue.edu

This paper presents a methodology for design optimization of thermoelectric-based waste heat recovery systems called thermoelectric generators (TEGs). The aim is to maximize the power output from thermoelectrics which are used as add-on modules to an existing gas-phase heat exchanger, without negative impacts, e.g., maintaining a minimum heat dissipation rate from the hot side. A numerical model is proposed for TEG coupled heat transfer and electrical power output. This finite-volume-based model simulates different types of heat exchangers, i.e., counter-flow and cross-flow, for TEGs. Multiple-filled skutterudites and bismuth-telluride-based thermoelectric modules (TEMs) are applied, respectively, in higher and lower temperature regions. The response surface methodology is implemented to determine the optimized TEG size along and across the flow direction and the height of thermoelectric couple legs, and to analyze their covariance and relative sensitivity. A genetic algorithm is employed to verify the globality of the optimum. The presented method will be generally useful for optimizing heat-exchanger-based TEG performance.

INTRODUCTION

The increasing demand for fuels, limited reserves, and environmental concerns motivate development of thermoelectric (TE) technology to convert thermal energy directly into electricity through solid-state thermoelectric devices.[1,2] Thermoelectric technology has the merit of no moving parts or emissions. Breakthroughs in materials, especially with nanotechnology, have revitalized the once-dormant thermoelectric research over the past several decades.[2–4] Thermoelectric materials are typically characterized by a figure of merit $Z = \alpha^2 \sigma / k$, a combination of the Seebeck coefficient α, thermal conductivity k, and electrical conductivity σ. For the performance of a thermoelectric generator (TEG), the power output is the first parameter to consider. However, there are other criteria[5,6] pertaining to

specific applications, such as deep-space probes,[7] automobile engines,[8–18] turbomachinery,[19,20] industrial waste heat recovery,[21] solar heat generators,[22] and portable power outlets with fuel.

A wide temperature range is often encountered when using thermoelectric technologies, e.g., for waste heat recovery. Considerable efforts have been devoted to Bi/Sb-Te-based materials[23–25] due to their high figure of merit (ZT) up to temperature of about 250°C. Skutterudite is a favorable material in a higher temperature range of about 250°C to 550°C,[26,27] and half-Heusler[8,28,29] Si-Ge,[30] or oxide[31,32] thermoelectric materials for even higher temperatures. Synergizing these materials, varied module types along the flow path,[10,33] segmented thermoelectric couple (TEC) legs[11,34,35] (also called cascade design), or stacked modules are applied so that different materials operate in their own temperature ranges. Other considerations[36–38] include mechanical stress, pressure drop, temperature distribution, etc. Once the TE materials

have been chosen, geometric parameters, including TEC cross-section area and height and heat exchanger length and width, are the dominant factors in TEG performance.

Numerical simulation is an efficient approach for parametric study of TEG performance and optimization, being the focus of this work. TEGs have been modeled with varied sophistication to provide knowledge on the performance of TEG designs. Earlier work modeled the heat exchanger using the Effectiveness-Number of Transfer Units (ϵ-NTU) method.[39] A one-dimensional (1-D) model along the flow path with given heat transfer coefficient provided knowledge on local hot- and cold-side temperatures.[40,41] Three-dimensional (3-D) modeling for a jet impingement heat exchanger was established to investigate heat transfer enhancement of a TEG.[42] Thermal resistor network analysis for thermoelectric modules (TEMs) is often used for computational efficiency, in which the power output can be obtained from the junction temperatures[22,40,43] by passing an equivalent resistor,[33,41] or more rigorously by applying the quadrupole method.[44] Integral properties[45] and meshed models[42,45,46] for TEC give more accurate results for TEM performance. However, the latter is computationally expensive for a full-sized TEG model. A transient model was also developed for simulating variable working conditions.[11]

In general, design optimization can be difficult when multiple mechanisms influence the performance with similar magnitudes. Although generating sufficient information, simply running through all possible combinations of parameters[33] is too expensive when many parameters are to be investigated. As such, genetic algorithms (GAs)[47,48] are popular in many thermal system design problems,[49,50] including for TEGs.[51,52] However, the data obtained during GA optimization are generally not suitable for visualization or sensitivity analysis. The response surface methodology (RSM),[52,54] by fitting the performance response to design variables, only requires computation of a few data to obtain the optimum, and the fit function during RSM calculations is available for sensitivity analysis.[51,52] However, RSM itself does not guarantee finding the global optimum.

In this study, we consider implementing thermoelectric technology in an existing gas-phase heat exchanger (i.e., in power plants), and the constraints of a minimum required heat dissipation rate from the hot side and limits on the total dimensions of the TEG. Design parameters of the heat exchanger area A_{HEX}, aspect ratio (AR), and height of TE leg H_{TE} are studied, because of their dominant effects on the TEG performance. A combined RSM–GA optimization process is proposed to perform an efficient search for the optimum. The RSM is used for optimization, while the GA is to avoid local optimums. The method also shows the relative sensitivities and interactions of design parameters. The total power output is the objective function, i.e., to be maximized during optimization, among all the performance indicators. The constraints are treated as bounds, or inequalities to which the design is subject. Other criteria, for example, cost per watt, can also be considered by directly adding explicit penalty functions to the objective function. However, these are not considered in this work. Based on established TEG models,[33,41] the present study optimizes the size of the heat exchanger and height of TEC legs to achieve the maximum power output under the heat transfer and size constraints.

NUMERICAL MODELING

The baseline model is shown in Fig. 1. Hot air from a heat source and cold air at ambient temperature are pumped into a cross-flow heat exchanger. The inlet temperatures of the hot and cold channels are fixed in the current study, as listed in Table I. Conduction in the heat exchanger is assumed only within the copper walls (brown in Fig. 1). TEMs are allocated between the heat-exchanging surfaces. Two types of TEMs, bismuth telluride and multiple-filled skutterudite, are selected for lower and higher temperature regions, respectively. The rest is filled with insulation blankets. A steady-state working condition is studied. A similar design of TEG for a counter-flow heat exchanger is also investigated for comparison.

The computational model is adapted from Kumar et al.,[33,41] with modifications of the resistor network for two-dimensional (2-D) heat exchangers and convective heat transfer. The heat transfer coefficient h is chosen based on a typical intermittent corrugated plate heat exchanger.[55] h varies with the Reynolds number Re, and thus with the channel width d and mass flow rate $\dot{m}$ as given in Eq. 1. The subscript "0" denotes reference values according to the baseline design. The value 0.35 is from the
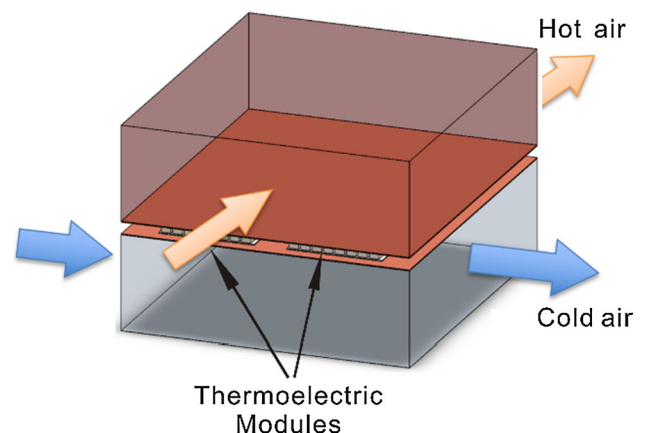

Fig. 1. Schematic of baseline design of TEG based on a gas-phase heat exchanger.

Table I. Baseline configuration

Parameter	Value	Unit
Inlet temperature (hot)	800	K
Inlet temperature (cold)	300	K
Heat transfer coefficient (hot)	2500	W/m^2-K
Heat transfer coefficient (cold)	2200	W/m^2-K
Mass flow rate (hot)	0.1	kg/s
Mass flow rate (cold)	0.1	kg/s
Air property	Ideal gas formulation	
Heat exchanger wall (copper) thickness	0.008	m
Thermal conductivity of copper	401	W m^{-1} K^{-1}
Heat exchanger area (A_{HEX})	0.12	m^2
Aspect ratio (AR)	0.75	–
Heat exchanger height	0.05	m
Height of TEC legs (H_{TE})	4	mm

Table II. TEM properties[33,41]

Parameter	Value	Unit
Skutterudite module		
Module (length, width, height)	(0.0508, 0.0508, 0.007)	(m, m, m)
TEC (number, length, width, height)	(32, 0.004, 0.004, 0.004)	(–, m, m, m)
$\varepsilon_{\mathrm{Module}}$ (ceramic)	0.55	–
Bismuth telluride		
Module (length, width, height)	(0.04013, 0.04013, 0.004)	(m, m, m)
TEC (number, length, width, height)	(127, 0.002, 0.002, 0.002)	(–, m, m, m)
$\varepsilon_{\mathrm{Module}}$ (ceramic)	0.55	–
Thermal grease (Grafoil laminate) thickness	0.001	m
Thermal grease conductivity	5	W m^{-1} K^{-1}
Thermal insulation (Min-K, Morgan Advanced Materials Inc.) thickness	0.002	m
Thermal insulation conductivity	0.0334	W m^{-1} K^{-1}
$\varepsilon_{\mathrm{Insulation}}$	0.75	–

regression of a similarly structured heat exchanger.[55]

$$h = h_0 \left(\frac{\mathrm{Re}}{\mathrm{Re}_0}\right)^{0.35} = h_0 \left(\frac{\dot{m}d_0}{\dot{m}_0 d}\right)^{0.35}. \quad (1)$$

The aspect ratio (AR) is defined as the ratio between the length along the hot air flow direction and that across the hot air flow direction. The parameters of the two types of TEMs and packaging are presented in Table II. This model assumes that TEMs cover 80% of the total area, and the rest is covered by insulation material. The model considers both conduction and radiation, where ε is the emissivity of ceramic/insulation surfaces.

The thermoelectric properties of filled skutterudite and Bi$_2$Te$_3$ are taken from Refs. 56–58. In the calculations, thermoelectric properties are calculated based on the integral average[45] at given junction temperatures T_{H} and T_{C}. The Seebeck coefficient α, for example, is expressed as

$$\bar{\alpha}_{n,p}(T_{\mathrm{H}}, T_{\mathrm{C}}) = \frac{\int_{T_{\mathrm{C}}}^{T_{\mathrm{H}}} \alpha_{n,p}\,\mathrm{d}T}{T_{\mathrm{H}} - T_{\mathrm{C}}}. \quad (2)$$

OPTIMIZATION METHODS

The response surface methodology (RSM)[53,54] is a collection of statistical techniques for modeling and analyzing problems in which the response of interest is affected by several variables. RSM has been used to analyze both experimental and simulation results. By fitting the results of a limited number of sample points, a response model can be developed. Optimization and sensitivity analysis can be achieved through this model.

In a physical model, as shown in Eq. 3, objective functions y_j (total number p) are determined by factors x_i (total number k), forming p number of k-dimensional surfaces in $(k + 1)$-dimensional space. In this study, the total power output is assigned to

be the objective function ($p = 1$), and the $k = 3$ factors are the heat exchanger area A_{HEX}, the aspect ratio AR, and the TE leg height H_{TE}. Possible combinations of these three factors are referred to as the design space, and any combination is called a design. The upper and lower limits of each factor are listed in Table III. The minimum heat dissipation rate from the hot side is set to 20 kW (Table III). These define the design space for this study.

$$y_j = f_i(x_1, \ldots, x_k) + \epsilon; \, j = 1, \ldots, p. \qquad (3)$$

Because of the lack of analytical solutions, the response model f is obtained by fitting simulation results with certain types of functions, and the error ϵ accounts for both numerical and fitting errors. Instead of calculating the absolute value, we use the Pearson correlation coefficient r^2 to show the relative significance of fitting error.

A large amount of data and a complicated fitting function are usually required to perform fitting for the entire design space. To simplify, we use either linear (Eq. 4) or second-order (Eq. 5) polynomials as the local fitting function at a design's neighborhood. The fitting coefficients β are obtained by the least-squares method.

$$f = \beta_0 + \sum_{i=1}^{3} \beta_i x_i, \qquad (4)$$

$$f = \beta_0 + \sum_{i=1}^{3} \beta_i x_i + \sum_{i=1}^{3} \beta_{ii} x_i^2 + \sum_{1 \le i < j \le 3} \beta_{ij} x_i x_j. \qquad (5)$$

The locally fit model is only valid within a small region of the design space. We select appropriate steps for the factors Δx_i so that the response model is fit, and thus valid, within the 3-D design region of $[x_i^n - \Delta x_i, x_i^n + \Delta x_i]$. The superscript "$n$" indicates the nth step during the optimization process. The steps also determine the updating of the design x_i^n during the optimization process; i.e., the differences of x_i^n and x_i^{n+1}, or two x_i^n between two consecutive substeps (described later in steepest ascent) are less than or equal to Δx_i. The choice of steps is a balance of resolution and convergence speed, also regarding the size limitation for manufacturability. For this study, the step selections are listed in Table III.

To obtain an effective and efficient fitting model around a design, the method of design of experiments (DOE)[54] is used. In one DOE set, different values of a factor, called levels, are used; For example, a three-level DOE for H_{TE} centered at the baseline design is $H_{\text{TE}} = 3.8\,\text{mm}, 4.0\,\text{mm}, 4.2\,\text{mm}$ according to its step size. Moreover, instead of running through all combinations of the three-factor three-level DOE, numerical simulation is only performed for the design points shown in Fig. 2, and the results can still produce an effective fitting function. The Box–Behnken design (Fig. 2a) and the central composite design (CCD) (Fig. 2b) can be applied to both the first- and second-order model. In these design patterns, the CCD has $2 \times k$ outreaching levels, shown as the six nodes out of the cube ($k = 3$) in Fig. 2b, to obtain better prediction.[54] In each DOE for fitting, the center level is taken according to the existing design. The +1 and −1 levels (Fig. 2a) for each factor are given by $x_i^0 + \Delta x_i$ and $x_i^0 - \Delta x_i$, and the outreaching levels for CCD (Fig. 2b) are chosen as $x_i^0 \pm 1.5\Delta x_i$.

RSM optimization operates in a sequential manner. The initial design, possibly being far from the optimum, is fit with the linear model and optimized with steepest ascent, i.e., finding the gradient of the local fitting function ∇f, and generating new designs according to its direction until the increment of the objective function of each step is less than 30% of that of the first step. One step of each factor in steepest ascent takes at most the step size defined earlier. This process provides a faster convergence rate, since it allows the design parameters to change by multiple steps after one fitting. The response surface is fit with the second-order model when it is closer to the optimum. The second-order model is also used for sensitivity analysis. In some problems, the objective function (the power output in this study) will be much higher when two factors have a particular relation, and much lower when they are out of the relation. This kind of response is called a ridge system[54] due to the shape of the response surface, indicating a particular interaction mechanism of factors dominating the performance. A ridge system can be identified by canonical transformation, and the transformation result can provide ideas to find the physical mechanism that explains how the certain combination of factors dominates the performance. In this study,

Table III. Design space and its discretization

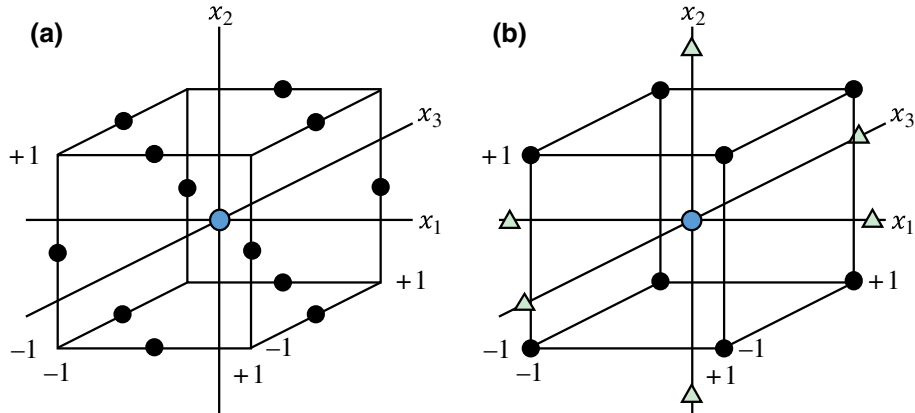| Factor	Unit	Step	Lower Limit	Upper Limit	GA Digits
A_{HEX}	m^2	0.02	0.08	0.4	6
ln(AR)	–	0.05	−0.7	0.7	6
H_{TE}	mm	0.2	1.5	8	6
Minimum heat dissipation 20 kW					

Fig. 2. Design of experiments for $k = 3$: (a) Box–Behnken design, and (b) central composite design.

A_{HEX} is one of the dominant factors for the power output, since it directly determines the total heat transfer rate. Based on this consideration, A_{HEX} and the AR are chosen as the factors instead of length and width of the heat exchanger channels (another ridge system is discussed below).

A genetic algorithm[47,48] is used as a global optimization tool to verify the globality of the RSM results. Inspired by evolution and natural selection, a particular design is referred to as an individual, its objective function as fitness, and the group of individuals as the population of one generation. The design space is discretized into binary genome series, indicated by the GA digits in Table III. New individuals are reproduced by combining genomes of the best individuals selected from the previous generation. This process, called crossover, preserves the possible features with better fitness, i.e., higher power output in this case. Diversity is achieved by a mutation process that randomly flips several binary digits of genomes to create new individuals to avoid local optimums. When used together with RSM, GA treats only the central nodes of designs in each DOE step as individuals to produce diverse designs of central nodes. The optimization process is still directed by the single-step RSM results, though GA is applied.

The procedure for the combined RSM–GA optimization is shown in the flowchart in Fig. 3 and described as follows: Initially, ten designs including the baseline design are generated, forming the first generation. The number of individuals is chosen based on the prior knowledge that the response surface has few local maxima, as several trials from different initial designs with RSM only gave the same optimum design. The response surface in the neighborhood of each individual is fit only once per generation. It is first fit with the linear model and optimized by steepest ascent. The second-order model is used when the power output of the design at the center point is higher than all other points on the edge, or when the linear model shows poor goodness of fit, $r^2 < 0.85$. Then, the next generation

is formed based on the nearest neighbors in the GA discretized design space of the steepest ascent results and the crossover and mutation rules. In each step, designs close to each other merge into one, and designs giving heat dissipation lower than the constraint are naturally selected out. GA stops when three successive iterations give improvement smaller than a given tolerance ($\Delta P < 5$ W). The response surface in the neighborhood of the optimized design in the last generation is then fit using the second-order model, and additional iterations are carried out until the power output predicted by the second-order model is within a given tolerance ($\Delta P < 0.1$ W).

RESULTS AND DISCUSSION

According to similar works[18,47] and our initial calculation results, the grid independence of the 2-D heat exchanger model is satisfactory when the grid size is smaller than 3 mm. On the other hand, the validity of the 1-D conduction thermal resistor network model for the TEC legs requires small temperature gradient across the cross-section of a leg, which is true for all the cases in this study. The leg cross-section size of Bi_2Te_3 (2 mm $\times$ 2 mm, Table II) is chosen to be the grid size for calculation.

Figure 4 illustrates the results of the combined RSM–GA optimization process. In Fig. 4a, for the counter-flow TEG case, the first 20 pairs of circles and diamonds show, respectively, the best individuals of each generation and the averaged performance of individuals in each generation. The converging trend of the averaged performance indicates that the global response surface is rather smooth. It is also observed that the change between iterations is smaller when the output power is closer to the neighborhood of the optimum. In fact, the global response surface in the current study is a highly ridged system. The larger curvature of the response surface model at the ridge near the optimum results in poor fitting of the linear model, so we use the second-order model to approach the optimum in the combined optimization process. The
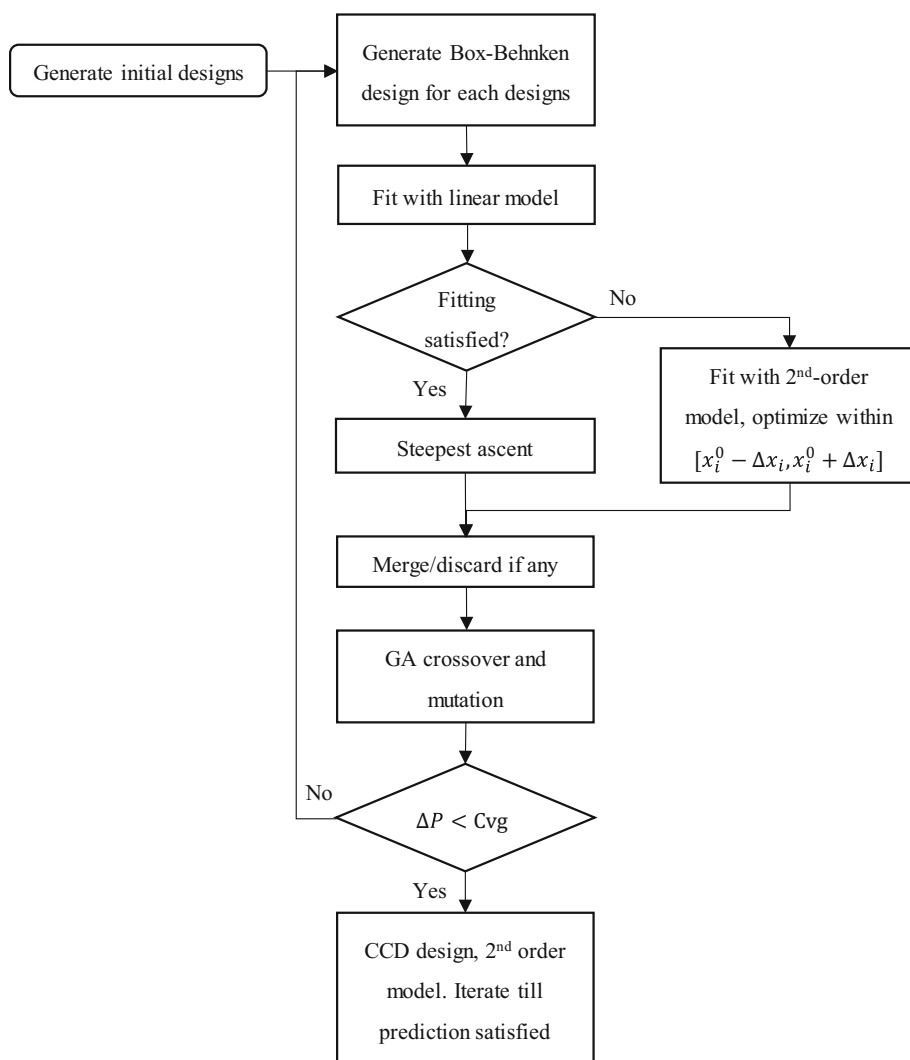
Fig. 3. Flowchart of combined RSM–GA optimization.

last four circles represent results of the optimization process using the second-order model for response surface fitting. The response surface is well fit at the optimum, with $r^2 = 0.94$. The optimized design for the counter-flow case has $A_{HEX} = 0.38\,m^2$, AR = 2.0, and $H_{TE} = 8.0\,mm$, giving a power output of 1.454 kW and a heat dissipation rate of 27.42 kW. The masses of skutterudite and Bi_2Te_3 are 3.2 and 2.7 kg, respectively.

A similar convergence of optimization results is shown in Fig. 4b for the cross-flow TEG. The converging trend of averaged performance towards the best individuals is also noticeable, but not as much as the case for the counter-flow TEG. This indicates that some individuals have much worse performance. The response surface forms a steeper peak in the neighborhood of the optimum, and the high-performance designs exist in a smaller region. This phenomenon can be conceptually understood based on the fact that a random combination of cross-flow TEG parameters is very likely to reduce

the higher power density region and result in low power output. The higher merging ratio during the RSM–GA process also implies this phenomenon, because individuals are more likely to gather in the design space when high-performance designs lie in a more confined region. The response surface is fit at the optimum with $r^2 = 0.90$. The optimized design for the cross-flow TEG is $A_{HEX} = 0.33\,m^2$, AR = 1.2, and $H_{TE} = 8.0\,mm$, giving a power output of 1.298 kW and a heat dissipation rate of 23.43 kW. The masses of skutterudite and Bi_2Te_3 are 2.8 and 2.4 kg, respectively.

The response surfaces in the neighborhood of the optimum are visualized in Figs. 5 and 6. In each plot, one of the three parameters is fixed at the value of the optimized design. The response models are developed by fitting the numerical results in regions larger than those defined by the step sizes, introducing limited fitting errors ($r^2 > 0.85$ for both cases), to illustrate the interaction and sensitivity of factors in these larger regions.
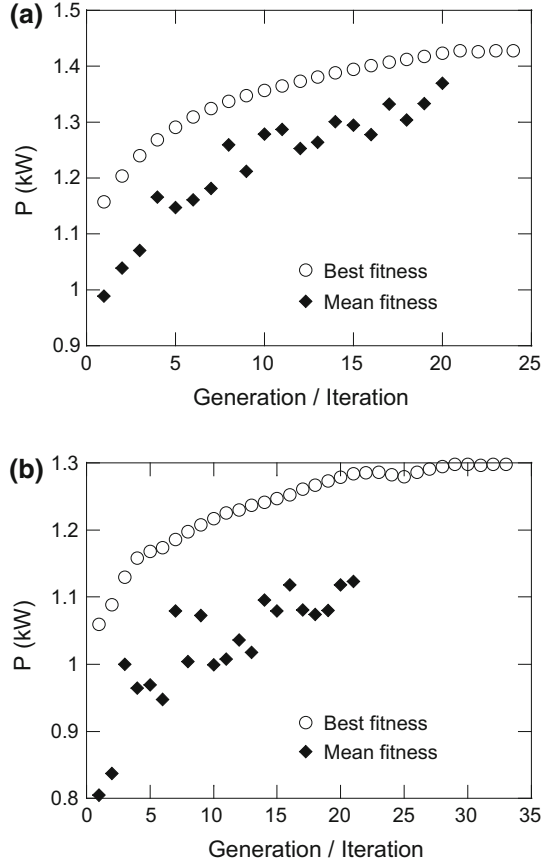
Fig. 4. Convergence of combined algorithm: (a) counter-flow TEG and (b) cross-flow TEG.

It can be seen in Fig. 5a that, by selecting the area A_{HEX} and the aspect ratio (AR) of the heat exchanger, instead of the lengths along and across the flow, as the design parameters, the objective function is close to canonical form. The gradients and contour lines are approximately parallel or perpendicular to the parameter axes. Thus, Fig. 5a clearly shows that, at given H_{TE}, A_{HEX} has an optimized value, which is approximately independent of AR. The power output increases with the aspect ratio, because higher aspect ratio results in larger velocity in the heat exchanger and thus enhanced heat transfer. This selection of parameters also improves the performance of the GA, since the crossover process is more efficient when the genomes represent orthogonal factors. The statements above are also true for the cross-flow TEG in Fig. 6a, except that the AR is much less sensitive than A_{HEX}. This is because, when convective heat transfer is enhanced by the flow speed on one side, it is reduced on the other side.

Another ridge system can be observed from Figs. 5b and 6b. Here, the power output is sensitive to both A_{HEX} and H_{TE}. A synergic increase of A_{HEX} and H_{TE} results in larger power output, while either increasing or decreasing one parameter with the other fixed leads to lower power output. Roughly,
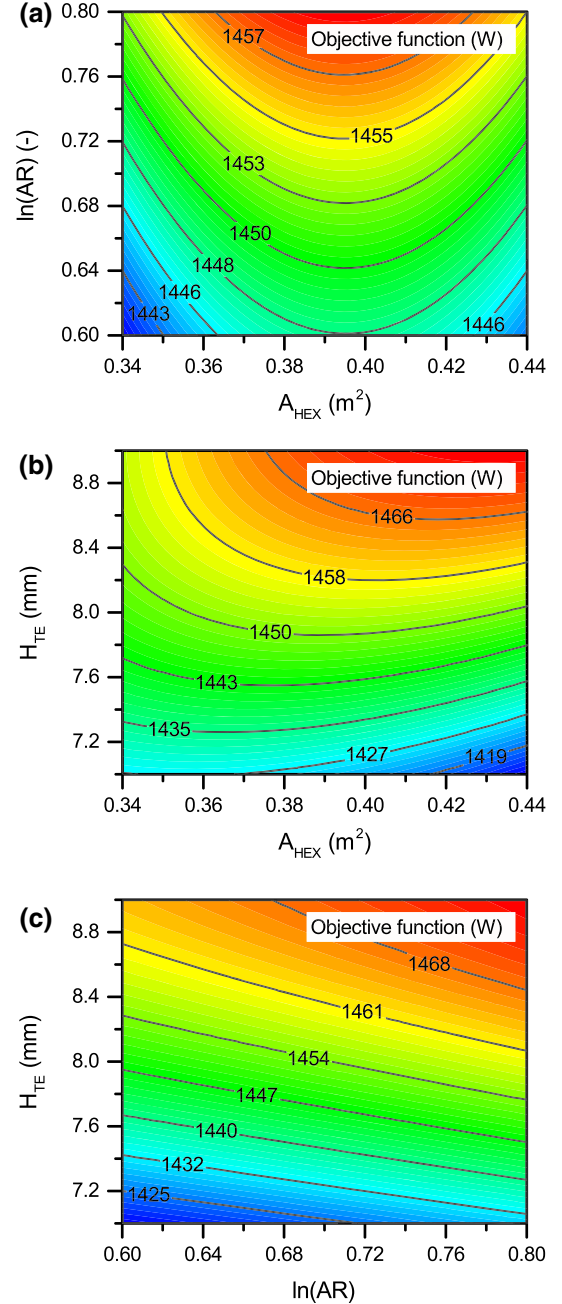

Fig. 5. 2-D projections of response surface near optimum for the counter-flow TEG: (a) A_{HEX}–AR response, (b) A_{HEX}–H_{TE} response, and (c) AR–H_{TE} response.

there is a line in the design space along whose direction the response surface has the smallest curvature and directional derivative. The optimum is expected to be the intersection of this line and the preset limits. The optimization under the specific constraints leads H_{TE} to its upper limit for both types of TEG. Also, we can simply search along this line for other optimums under different dimensional constraints; For example, introducing cost per watt as a penalty function can avoid the optimized A_{HEX} and H_{TE} becoming too large.
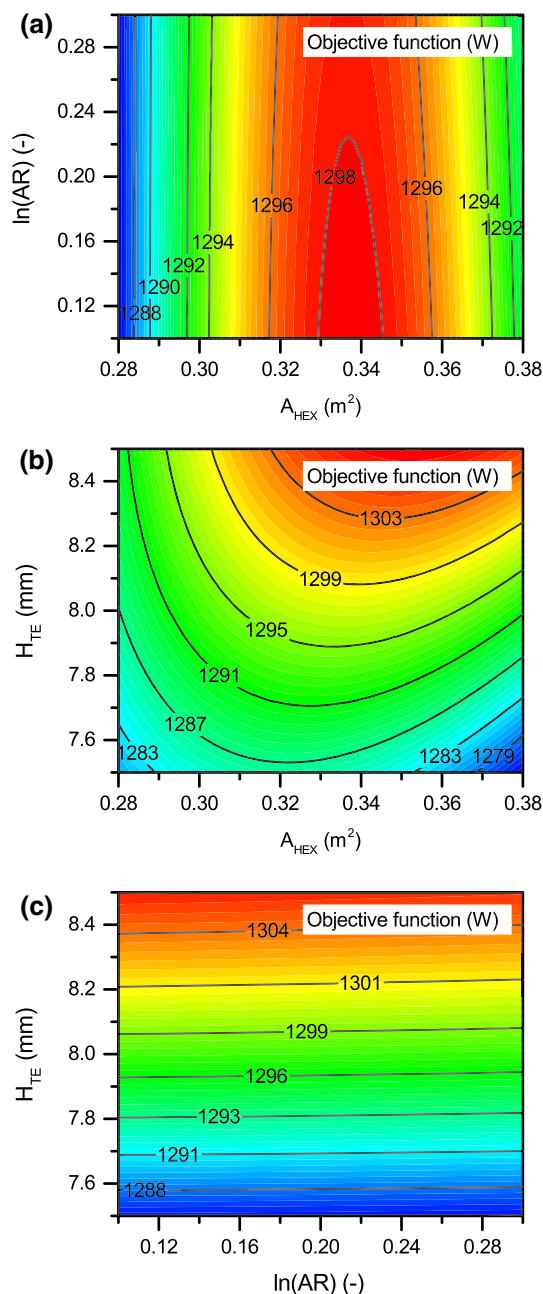
Fig. 6. 2-D projections of response surface near optimum for the cross-flow TEG: (a) A_{HEX}–AR response, (b) A_{HEX}–H_{TE} response, and (c) AR–H_{TE} response.

Fig. 7. Performance of optimized counter-flow TEG: (a) temperature distribution along the flow and (b) length-based power density. $A_{HEX} = 0.38$ m^2, AR = 2.0, $H_{TE} = 8.0$ mm.

Fig. 8. Performance of TEMs between heat reservoirs with different H_{TE} ($T_{hot,\ reservoir} = 800$ K, $T_{cold,\ reservoir} = 300$ K).

In the neighborhood of the optimum, H_{TE} appears to have a similar level of sensitivity in comparison with A_{HEX} and is more sensitive than the aspect ratio, as shown in Figs. 5c and 6c. However, during steepest ascent, the gradient fraction for H_{TE} can be over two orders of magnitude larger than that for the area, and nearly four orders of magnitude larger than that for the aspect ratio. When the TEC resistance roughly equals the package and interface resistance, the junction temperature difference is very sensitive to H_{TE}. Thus, a small change of H_{TE}
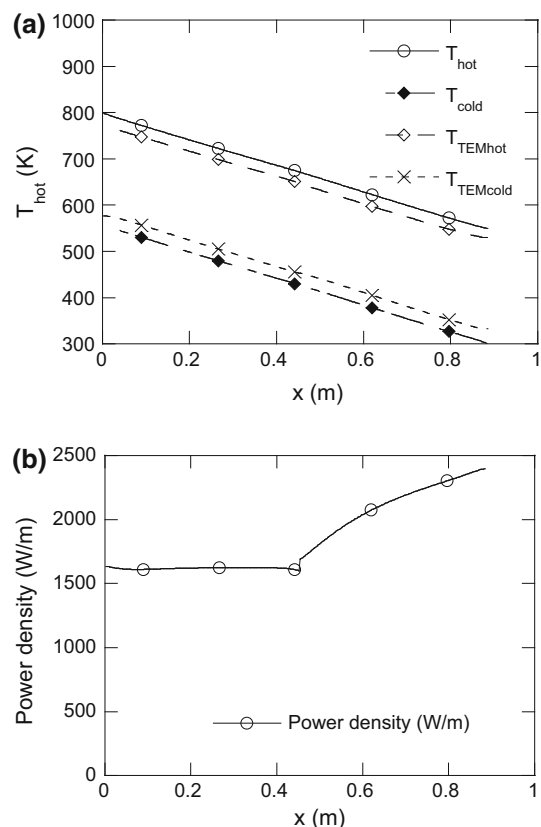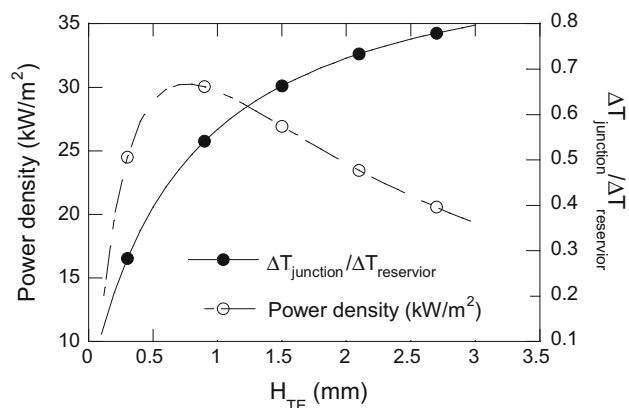
makes a noticeable difference in the power output, and a small step size should be used to investigate the factor H_{TE}. In this work, the step size of the TEC leg height is set to 0.2 mm, considering the accuracy that can be achieved in manufacturing.

The temperature distribution and power density of the optimized design for both types of TEG are shown in Figs. 7 and 8. As shown in Fig. 7a, the temperature difference between the hot and cold sides is nearly a constant. The junction temperature
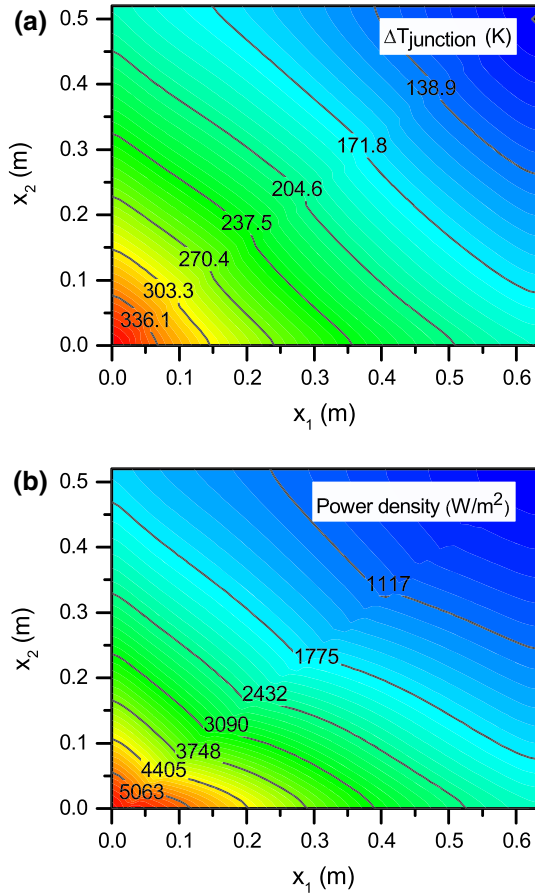
Fig. 9. Performance of the optimized cross-flow TEG: (a) junction temperature difference and (b) area-based power density. $A_{HEX} = 0.33$ m^2, AR = 1.22, $H_{TE} = 8.0$ mm.

decreases. Since the temperature difference is almost constant, the Carnot efficiency is higher when the average temperature is lower. The lower Carnot efficiency is balanced by the higher ZT of skutterudite in the part at higher temperature. On the other hand, ZT of bismuth telluride does not vary much with temperature in its operating temperature range. Thus, the power density is higher in the colder region, as shown in Fig. 7b.

One phenomenon noted from the temperature distribution of the cross-flow heat exchanger, as shown in Fig. 9, is that the temperature difference is larger at one corner than at the other three corners, and thus generates more power. An improper combination of A_{HEX} and H_{TE} could result in a smaller high-power-density region, thus greatly reducing power generation.

CONCLUSIONS

A combined RSM–GA optimization method is developed based on numerical models of TEGs. The optimization algorithm brings rigor to the trial-and-error empirical design and efficiency to direct search through the design space. Cases of TEGs with cross-flow and counter-flow heat exchangers are studied. Power outputs are maximized with the required heat dissipation from the hot side. The response relations including sensitivity and inter-action of factors are also analyzed. The results show that the combined algorithm is applicable for designs of TEGs and similar problems with multiple dominating mechanisms. In addition, the sensitivity and interaction analysis shows the effects of varying factors on the power output independently and concurrently, which has the potential to obtain optimized designs under different constraints with less calculation. We also emphasize that the optimization results provide intuition and reference for future designs.

difference is slightly smaller because of the axial conduction. H_{TE} exhibits a trade-off in that a larger leg height results in a larger junction temperature difference but lower heat flow rate and thus less power output, and vice versa. When the hot- and cold-side temperatures of the heat reservoirs are fixed, the optimized H_{TE} has a thermal resistance approximately equal to that of the interface and packaging materials; i.e., the junction temperature difference is approximately half of that between the reservoirs (Fig. 8). Single-variable optimization of H_{TE} with other parameters fixed also shows the existence of an optimized H_{TE}. However, when A_{HEX} and H_{TE} are free to vary at the same time, an increment of the area can always provide a higher heat flux and an increase of H_{TE} can always give a larger temperature difference. H_{TE} is optimized to its upper limit in this study.

Figure 7b shows the output power density along the flow direction. Its trends differ according to the different types of TEM. The hotter part of the TEG is equipped with filled-skutterudite modules that generate approximately constant power along the flow. The Bi$_2$Te$_3$ modules are at the colder part, and the power density increases as the mean temperature

REFERENCES

1. H.J. Goldsmid, in *CRC Handbook of Thermoelectrics*, ed. D.M. Rowe (CRC Press, Abingdon, 1995), p. 1.
2. D.M. Rowe, in *Thermoelectrics Handbook: Macro to Nano*, ed. D.M. Rowe (CRC Press, Abingdon, 2006), p. 1-1-14.
3. M.S. Dresselhaus, G. Chen, M.Y. Tang, R.G. Yang, H. Lee, D.Z. Wang, Z.F. Ren, J.-P. Fleurial, and P. Gogna, *Adv. Mater.* 19, 1043 (2007).
4. D.D. Klug and J.S. Tse, in *Thermoelectrics Handbook: Macro to Nano*, ed. D.M. Rowe (CRC Press, Abingdon, 2006), p. 8-1-28.
5. D.M. Rowe and G. Min, *J. Power Sources* 73, 193 (1998).
6. S.K. Yee, S. LeBlanc, K.E. Goodson, and C. Dames, *Energy Environ. Sci.* 6, 2561 (2013).

7. B.C. Blanke, J.H. Birden, K.C. Jordan, and E.L. Murphy, *Nuclear Battery-Thermocouple Type Summary Report, AEC Research and Development Report,* Monsanto Research Corporation, MLM-1127 (1962). http://www.osti.gov/scitech/biblio/4807049.

8. D.T. Crane and J.W. Lagrandeur, *J. Electron. Mater.* 39, 2142 (2010).

9. Y. Zhang, M. Cleary, X. Wang, N. Kempf, L. Schoensee, J. Yang, G. Joshi, and L. Meda, *Energy Convers. Manage.* 105, 946 (2015).

10. N. Espinosa, M. Lazard, L. Aixala, and H. Scherrer, *J. Electron. Mater.* 39, 1446 (2010).

11. D.T. Crane, *J. Electron. Mater.* 40, 561 (2011).

12. J. Yang, in *ICT 2005. 24th International Conference on Thermoelectrics* (2005), pp. 170–174.

13. J. Yang and T. Caillat, *MRS Bull.* 31, 03 (2006).

14. J. Yang and F. Stabler, *J. Electron. Mater.* 38, 1245 (2009).

15. E.F. Thacher, B.T. Helenbrook, M.A. Karri, and C.J. Richter, *Proc. Inst. Mech. Eng. D* 221, 95 (2007).

16. M.A. Karri, E.F. Thacher, and B.T. Helenbrook, *Energy Convers. Manage.* 52, 1596 (2011).

17. D. Crane, J. Lagrandeur, V. Jovovic, M. Ranalli, M. Adldinger, E. Poliquin, J. Dean, D. Krossakovski, B. Mazar, and C. Maranville, *J. Electron. Mater.* 42, 1582 (2013).

18. C.-T. Hsu, G.-Y. Huang, H.-S. Chu, B. Yu, and D.-J. Yao, *Appl. Energy* 88, 1291 (2011).

19. P. Yodovard, J. Khedari, and J. Hirunlabh, *Energy Sources* 23, 213 (2001).

20. K. Yazawa, Y.R. Koh, and A. Shakouri, *Appl. Energy* 109, 1 (2013).

21. T. Ota, C. Tokunaga, and K. Fujita, in *ICT 2005. 24th International Conference on Thermoelectrics* (2005), pp. 335–338.

22. S.A. Omer and D.G. Infield, *Sol. Energy Mater. Sol. Cells* 53, 67 (1998).

23. S. Scherrer and H. Scherrer, in *CRC Handbook of Thermoelectrics*, ed. D.M. Rowe (CRC Press, Abingdon, 1995), pp. 211–237.

24. Y. Wang, B. Qiu, A.J. McGaughey, X. Ruan, and X. Xu, *J. Heat Transfer* 135, 091102 (2013).

25. C.V. Manzano, V. Abad, M.M. Rojo, Y.R. Koh, S.L. Hodson, A.M.L. Martinez, X. Xu, A. Shakouri, T.D. Sands, T. Borca-Tasciuc, and M. Martin-Gonzalez, *Sci. Rep.* 6, 19129 (2016).

26. B.C. Sales, D. Mandrus, and R.K. Williams, *Science* 272, 5266 (1996).

27. Y. Wang, X. Xu, and J. Yang, *Phys. Rev. Lett.* 102, 175508 (2009).

28. M. Schwall and B. Balke, *Appl. Phys. Lett.* 98, 042106 (2011).

29. P.H. Ngan, N. van Nong, L.T. Hung, B. Balke, L. Han, E.M. Hedegaard, S. Linderoth, and N. Pryds, *J. Electron. Mater.* 45, 594 (2016).

30. C.B. Vining, in *CRC Handbook of Thermoelectrics*, ed. D.M. Rowe (CRC Press, Abingdon, 1995), pp. 329–337.

31. K. Koumoto, in *Thermoelectrics Handbook: Macro to Nano*, ed. D.M. Rowe (CRC Press, Abingdon, 2006), p. 35-1-15.

32. J. He, Y. Liu, and R. Funahashi, *J. Mater. Res.* 26, 1762 (2011).

33. S. Kumar, S.D. Heister, X. Xu, J.R. Salvador, and G.P. Meisner, *J. Electron. Mater.* 42, 944 (2013).

34. B.W. Swanson, E.V. Somers, and R.R. Heikes, *J. Heat Transfer* 83, 77 (1961).

35. K. Matsubara, in *Proceedings ICT'02. Twenty-First International Conference on Thermoelectrics* (2002), pp. 418–423.

36. X. Meng and R.O. Suzuki, *J. Electron. Mater.* 44, 1469 (2015).

37. Y.D. Deng, X. Liu, S. Chen, and N.Q. Tong, *J. Electron. Mater.* 42, 1634 (2013).

38. M. Musial, M. Borcuch, and K. Wojciechowski, *J. Electron. Mater.* 45, 1517 (2016).

39. J. Esartea, G. Min, and D.M. Rowe, *J. Power Sources* 93, 72 (2001).

40. J. Yu and H. Zhao, *J. Power Sources* 172, 1 (2007).

41. S. Kumar, S.D. Heister, X. Xu, J.R. Salvador, and G.P. Meisner, *J. Electron. Mater.* 42, 665 (2013).

42. K.S.-Y. Hu, X. Chi, T. Shih, and H.J. Schock, in *47th AIAA Aerospace Sciences Meeting including the New Horizons Forum and Aerospace Exposition* (2009), pp. 2009–1210.

43. Y.Y. Hsiao, W.C. Chang, and S.L. Chen, *Energy* 35, 1447 (2010).

44. Y. Ezzahri, S. Dilhaire, S. Grauby, L. D. Patiño-Lopez, W. Claeys, Y. Zhang, Z. Bian, and A. Shakouri, in *ICT 2005. 24th International Conference on Thermoelectrics* (2005), pp. 256–260.

45. S. Kumar, S.D. Heister, X. Xu, and J.R. Salvador, *J. Electron. Mater.* 44, 3627 (2015).

46. R. Harris, T. Hogan, H.J. Schock, and T. I. P. Shih, in *Aerospace Sciences Meeting, AIAA Paper, 0575* (2006).

47. K.F. Man, K.S. Tang, and S. Kwong, *IEEE Trans. Ind. Electron.* 43, 519 (1996).

48. D. Whitley, *Stat. Comput.* 4, 65 (1994).

49. L. Gosselin, M. Tye-Gingras, and F. Mathieu-Potvin, *Int. J. Heat Mass Transfer* 52, 2169 (2009).

50. G. Fabbri, *Int. J. Heat Mass Transfer* 40, 2165 (1997).

51. C.Q. Su, C. Huang, Y.D. Deng, Y.P. Wang, P.Q. Chu, and S.J. Zheng, *J. Electron. Mater.* 45, 1464 (2016).

52. J.W. Qiang, C.G. Yu, Y.D. Deng, C.Q. Su, Y.P. Wang, and X.H. Yuan, *J. Electron. Mater.* 45, 1679 (2016).

53. G.E.P. Box and J.S. Hunter, *Ann. Math. Stat.* 28, 195 (1957).

54. D.C. Montegomery, *Design and Analysis of Experiments*, 8th ed. (New York: Wiley, 2012), pp. 478–553.

55. W.M. Kays and A.L. London, *Compact Heat Exchangers*, 3rd ed. (New York: McGraw-Hill, 1993), p. 195.

56. G. Rogl, A. Grytsiv, E. Bauer, P. Rogl, and M. Zehetbauer, *Intermetallics* 18, 57 (2010).

57. X. Tang, Q. Zhang, L. Chen, T. Goto, and T. Hirai, *J. Appl. Phys.* 97, 093712 (2005).

58. X.B. Zhao, X.H. Ji, Y.H. Zhang, T.J. Zhu, J.P. Tu, and X.B. Zhang, *Appl. Phys. Lett.* 86, 062111 (2005).